

# Spontaneous time reversal symmetry breaking at individual grain boundaries in graphene

Kimberly Hsieh<sup>1,\*</sup>, Vidya Kochat<sup>1,5,\*</sup>, Tathagata Biswas<sup>1,6</sup>, Chandra Sekhar Tiwary<sup>2,7</sup>,  
Abhishek Mishra<sup>3</sup>, Gopalakrishnan Ramalingam<sup>4</sup>, Aditya Jayaraman<sup>1</sup>, Kamanio  
Chattopadhyay<sup>2</sup>, Srinivasan Raghavan<sup>3,4</sup>, Manish Jain<sup>1</sup> & Arindam Ghosh<sup>1,3</sup>

<sup>1</sup> Department of Physics, Indian Institute of Science, Bangalore 560 012, India

<sup>2</sup> Department of Materials Engineering, Indian Institute of Science, Bangalore 560 012, India

<sup>3</sup> Centre for Nano Science and Engineering, Indian Institute of Science, Bangalore 560 012, India and

<sup>4</sup> Materials Research Center, Indian Institute of Science, Bangalore 560 012, India\*

Graphene grain boundaries have attracted interest for their ability to host nearly dispersionless electronic bands and magnetic instabilities. Here, we employ quantum transport and universal conductance fluctuations (UCF) measurements to experimentally demonstrate a spontaneous breaking of time reversal symmetry (TRS) across individual GBs of chemical vapour deposited graphene. While quantum transport across the GBs indicate spin-scattering-induced dephasing, and hence formation of local magnetic moments, below  $T \lesssim 4$  K, we observe complete lifting of TRS at high carrier densities ( $n \gtrsim 5 \times 10^{12} \text{cm}^{-2}$ ) and low temperature ( $T \lesssim 2$  K). An unprecedented thirty times reduction in the UCF magnitude with increasing doping density further supports the possibility of an emergent frozen magnetic state at the GBs. Our experimental results suggest that realistic GBs of graphene can be a promising resource for new electronic phases and spin-based applications.

Structural disorder in graphene originates from defects classifiable into two categories - point defects (vacancies, Stone-Wales defects) and extended defects such as grain boundaries (GBs). Vacancies result in localized states close to zero energy leading to magnetic moment formation in graphene, experimentally confirmed by the observation of spin-split resonances in scanning tunneling microscopy (STM) at monovacancies [1], measurements of spin currents [2] and possibility of Kondo effect [3, 4]. GBs lead to local modification of graphene band structure by introducing weakly dispersing, nearly flat electronic bands with enhanced density of states (DOS), either at zero energy (translational GB(2,0)|(2,0)) [5, 6] or finite energies (tilt GB(5,0)|(3,3)) [7–9]. While preliminary studies projected GBs as detrimental to electronic transport [10–17], successive experiments showed that these drawbacks can be overcome by tailoring the growth conditions [18, 19]. Magnetotransport measurements across isolated GBs reveal enhanced weak localization (WL) compared to single-crystalline grains, indi-

cating stronger intervalley carrier scattering due to lattice disorder [10, 17]. However, a comprehensive study of the symmetry-breaking mechanisms at graphene GBs through direct measurements of universal conductance fluctuations (UCF) in the inter- and intra-grain regions has so far been lacking.

Magnetic ordering has been predicted at GBs, either by localization at non-trivially coordinated C-rings [7] or assisted by strain, *e.g.* in translational line defects with octagon-pentagon pairs [5, 6]. In realistic GBs realized during chemical vapour deposition (CVD) growth, nucleation centers grow independently and fuse in local bonding environment. Such GBs comprise multiple defect realizations, including vacancies, Stone-Wales defects, intermittent 1D line defects [12, 20], multi-membered C-rings [7, 21] etc., causing strong increase in charge carrier scattering and electronic noise [14, 18, 19]. Despite both numerical [5–7] and spectroscopic [8, 9, 20, 22] evidences of large enhancement in local DOS and spin-splitting, no tangible impact of *e-e* interaction at the GBs has so far been observed. This work combines quantum transport and UCF to probe local charge and spin excitations across individual graphene GBs. The UCF magnitude, determined by the symmetry of the underlying Hamiltonian via the Wigner-Dyson parameter  $\beta$  [23], reveals a full spontaneous lifting of the time reversal symmetry (TRS) in the GB region for  $T \lesssim 2$  K and  $n \gtrsim 5 \times 10^{12} \text{cm}^{-2}$ . The temperature and density-dependence of UCF links the TRS lifting to a frozen magnetic state arising from the GB defect sites.

We measured three devices (D1, D2 and D3) from CVD-synthesized graphene (Supplemental Material (SM) section S1), optimized to ensure partial fusion of crystallites (scanning electron micrograph in Fig. 1a). High-resolution transmission electron mi-

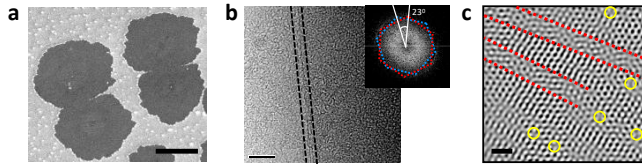


FIG. 1. **a**, Scanning electron micrograph of a typical pair of graphene grains with grain size  $\approx 15 \mu\text{m}$  forming a GB in between. Scale bar,  $10 \mu\text{m}$ . **b**, Bright field TEM image of the GB formed between two grains. Selected area electron diffraction (SAED) pattern in inset shows the misorientation angle between the grains  $\approx 23^\circ$ . Scale bar,  $5 \text{nm}$ . **c** HRTEM image of the GB region where line and point defects are outlined. Scale bar,  $1 \text{nm}$ .

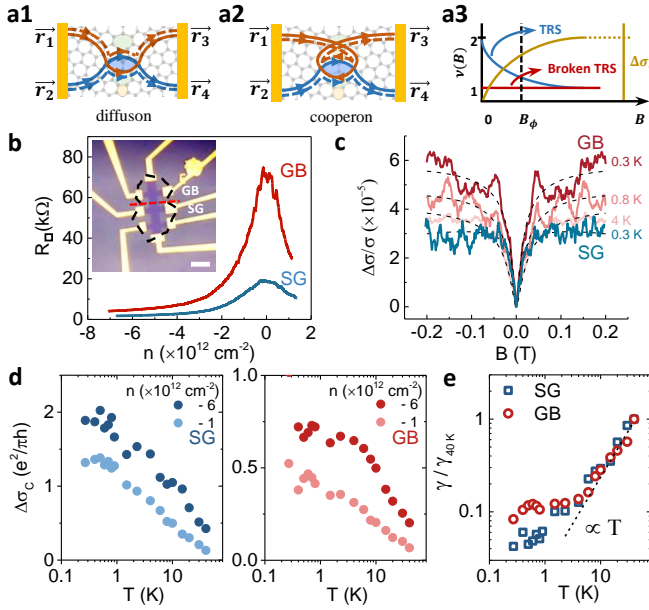


FIG. 2. **a**, Schematic showing **a1**, a pair of crossings representing diffusons, **a2**, a pair of crossings representing Cooperons, and **a3**, the expected behaviour of  $\nu(B)$  as a function of  $B$  for TRS-invariant and TRS-broken systems. **b**, Sheet resistance ( $R_{\square}$ ) as a function of gate voltage ( $V_{BG}$ ) for intra-grain (SG) and inter-grain (GB) regions of D1 at  $T = 0.3$  K. (Inset) Optical micrograph of a typical device. The morphology of the original pair of coalesced grains is shown (black line) along with the approximate GB location (red line). Scale bar,  $10 \mu\text{m}$ . **c**, Magnetoconductance measurements are shown for  $n = -6 \times 10^{12} \text{ cm}^{-2}$  at  $T = 0.3$  K for the SG region and  $T = 0.3, 0.8$ , and  $4$  K for the GB region, clearly exhibiting WL. Dashed lines correspond to HLN fits. **d**, Quantum correction to conductivity  $\Delta\sigma_c$  in units of  $e^2/\pi h$  plotted for both SG and GB regions as a function of  $T$  for  $n = -1 \times 10^{12} \text{ cm}^{-2}$  and  $-6 \times 10^{12} \text{ cm}^{-2}$ . **e**, Scattering rate  $\gamma$  normalized to its value  $\gamma_{40\text{K}}$  at  $T = 40$  K, plotted versus  $T$  for the SG and GB regions at  $n = -6 \times 10^{12} \text{ cm}^{-2}$  is shown, where the black dotted line indicates the temperature regime where Nyquist scattering dominates.

croscopy (HRTEM) (Fig. 1b) performed on a pair of similarly synthesized grains reveal an average width  $\sim 10$  nm of the disordered region, and a misorientation angle  $\approx 23^\circ$  between the parent crystallites. The GBs form a highly disordered region consisting of arrays of line dislocations and under-coordinated C-atoms (Fig. 1c) similar to that observed in STM and TEM studies [8, 9, 19, 20, 22].

Fig. 2a schematically describes the conceptual basis of our experimental approach. The quantum interference effect, that underpins both quantum correction to conductivity ( $\Delta\sigma_c$ ) and UCF ( $\langle\delta G_\phi^2\rangle$ ), depends on crossings of time-reversed path pairs as the electron (or hole) diffuses across the sample over  $\tau_D = L^2/D$ , the Thouless time, where  $L$  and  $D$  are the length of the system and carrier diffusivity, respectively. While  $\Delta\sigma_c$  is determined by the probability of single self-crossing, the

correlation function in  $\langle\delta G_\phi^2\rangle \sim \langle G(0)G(\tau)\rangle_\tau$  requires two spatially separated crossing points (thus involving larger number of defect sites), thereby defining closed loops encircled either in the same (diffusons) or opposite (Cooperons) senses with identical structure factors (Figs. 2a1 and 2a2). This has two important consequences: first, compared to  $\Delta\sigma_c$  ( $\sim \ln(\tau_D\gamma)$ ), the UCF magnitude  $\langle\delta G_\phi^2\rangle \sim (\tau_D\gamma)^{-2}$  is exponentially more sensitive to emergent dephasing processes in two dimensions, where  $\gamma$  is the dephasing rate, and thus a more suitable tool when the dephasing processes are confined within spatially restricted regions such as the GBs. Second, when TRS is lifted, usually by a transverse magnetic field  $B \gg B_\phi$ ,  $B_\phi$  being the field corresponding to one flux quantum threading a phase coherent cell, the Cooperon contribution is removed, decreasing  $\langle\delta G_\phi^2\rangle$  *exactly* by a factor of two. The reduction factor is protected by the symmetry of the underlying Hamiltonian, *i.e.*  $\langle\delta G_\phi^2\rangle \sim (e^2/h)^2/\beta$ , where  $\beta = 1$  for time reversal invariant systems (orthogonal ensemble), and  $\beta = 2$  when TRS is absent (unitary ensemble). For a time-reversal invariant system [24], a crossover function  $\nu(B)$  defined as

$$\nu(B) = \frac{N(B)}{N_\phi} = 1 + \frac{2}{b^2} \sum_{n=0}^{\infty} \frac{1}{[(n + \frac{1}{2}) + \frac{1}{b}]^3} \quad (1)$$

where  $b = 8\pi B(l_\phi)^2/(h/e)$  is the dimensionless magnetic field which captures the reduction in UCF as a function of  $B$  (Fig. 2a3). Here,  $N(B)$  and  $N_\phi$  are the values of  $\langle\delta G_\phi^2\rangle$  at  $B$  and at  $B \gg B_\phi$ , respectively. When TRS is spontaneously removed (magnetic systems),  $\nu(B)$  remains unaffected at the scale of  $B_\phi$ , as observed in ferromagnetic films [25].

For electrical transport, the graphene grains were transferred on to Si/SiO<sub>2</sub> substrates, patterned into Hall bars such that measurements across the GB and within single grain (SG) can be carried out simultaneously (Fig. 2b inset). The excess disorder in the GB region results in enhancement in the resistivity by a factor of  $\sim 2-5$  times that of the SG region depending on  $n$  (Fig. 2b) and a consequent suppression of the carrier mobility ( $\mu_{SG} \approx 480 \text{ cm}^2\text{V}^{-1}\text{s}^{-1}$  while  $\mu_{GB} \approx 220 \text{ cm}^2\text{V}^{-1}\text{s}^{-1}$ ). Magnetotransport measurements down to  $T = 0.3$  K for a fixed  $n$  ( $\approx -6 \times 10^{12} \text{ cm}^{-2}$ ) indicate enhanced WL correction at the GB region (Fig. 2c), signifying stronger intervalley scattering from short range lattice defects [10, 17, 26]. Fitting (dashed lines in Fig. 2c) the modified Hikami-Larkin-Nagaoka (HLN) expression for graphene [27] to magnetoconductance yields both the quantum correction to conductivity  $\Delta\sigma_c$  and the dephasing length  $l_\phi$  (Fig. S2a). The  $T$ -dependence of  $\Delta\sigma_c$  in Fig. 2d shows that the quantum correction behaves differently between SG (left) and GB (right) regions, especially at high  $n$ . In both cases, we find  $\Delta\sigma_c \propto \ln(T)$  at low  $n$ , as expected for diffusive non-magnetic conductors

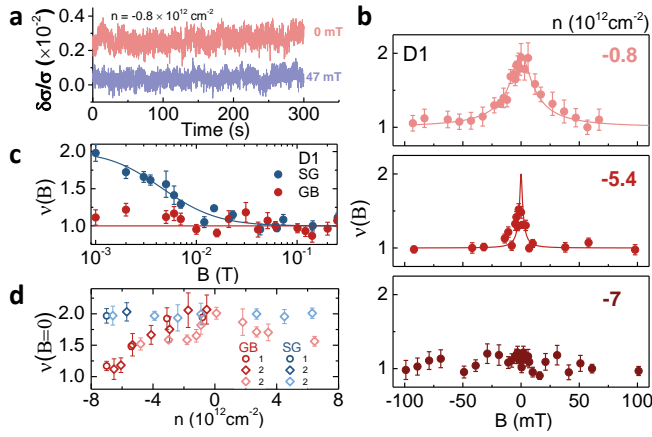


FIG. 3. **a**, Conductivity fluctuations for GB region of D1 at  $n = -0.8 \times 10^{12} \text{ cm}^{-2}$  for  $B = 0 \text{ mT}$  (pink) and  $B = 47 \text{ mT}$  (purple), clearly indicating a reduction in the fluctuation magnitude at  $B \gg B_\phi$ . **b**,  $\nu(B)$  plotted for three different  $n$  at  $T = 0.3 \text{ K}$  for D1 showing spontaneous TRS breaking at zero field as  $n$  is increased. Solid lines are fits to Eq. 1. **c**,  $\nu(B)$  for the SG and GB regions plotted at  $T = 0.3 \text{ K}$  for D1 at  $n = -7 \times 10^{12} \text{ cm}^{-2}$  indicating that spontaneous TRS breaking occurs only in the presence of a GB. **d**, Noise reduction factor  $\nu(B = 0)$  for the SG and GB regions of D1 (circles) measured at  $T = 0.3 \text{ K}$  (darker) and D2 (diamonds) at  $T = 0.3 \text{ K}$  (darker) and  $T = 4.5 \text{ K}$  (lighter) as a function of  $n$ .

where dephasing takes place via Nyquist scattering from  $e$ - $e$  interaction so that  $\gamma = D/l_\phi^2 \propto T$ . Direct evaluation of  $\gamma$  (Figs. 2e and S2b) from HLN fits confirm this proportionality with  $T$ . The quantum correction in the GB region at high  $n$  ( $\gtrsim 5 \times 10^{12} \text{ cm}^{-2}$ ) however deviates from this behaviour, where we find both  $\Delta\sigma_c$  (Fig. 2d, right panel) and  $\gamma$  (Fig. 2e) saturate below  $T \sim 7 \text{ K}$ .

Low temperature saturation of  $\gamma$  in metals is often attributed to inelastic processes from spin-flip scattering [28–30]. Neglecting electron-phonon scattering at such temperatures [31, 32], we can write  $\gamma = \gamma_{ee} + \gamma_s$ , where  $\gamma_{ee}$  is the  $e$ - $e$  induced scattering rate and  $\gamma_s$  is the spin-flip scattering rate due to dilute magnetic impurities. The observed saturation in  $\gamma$  at temperatures  $T \lesssim 7 \text{ K}$  can thus be explained from increasing Nyquist scattering ( $\gamma_{ee} \propto T$ ) countering the reduction in  $\gamma_s$  above the Kondo temperature  $T_K$  [33, 34]. Such an anomalous  $T$ -dependence of  $\gamma$  in the inter-grain region hints at the formation of magnetic moments that can interact at lower temperatures leading to frozen magnetic ordering [35]. However, the competing effects of localization and anti-localization due to graphene’s chiral charge carriers makes it ambiguous to detect or claim such possibilities using WL alone.

To complement quantum transport, we carried out UCF measurements in two different ways: (1) From slow time-dependent fluctuations in the conductance relating directly to the ensemble fluctuations of disorder configuration via ergodic hypothesis [24, 36–38] (Fig. 3,

SM section S4), and (2) by analyzing the reproducible and aperiodic fluctuations in  $G$  by tuning the Fermi energy (Fig. 4b, SM section S5). The time-dependent conductance fluctuations across the GB of D1 at  $n = -0.8 \times 10^{12} \text{ cm}^{-2}$  is plotted in Fig. 3a, clearly displaying a reduction in the relative magnitude of fluctuations at  $B = 0 \text{ T}$  and  $B = 47 \text{ mT}$  ( $\gg B_\phi$ ). Fig. 3b shows the  $B$ -dependence of  $\nu(B)$ , defined in Eq. 1, from  $\langle \delta G_\phi^2 \rangle$  evaluated from time-dependent conductance fluctuations in device D1 for three different  $n$  at the GB region. At low  $n$  ( $\approx 0.8 \times 10^{12} \text{ cm}^{-2}$ ),  $\nu(B)$  shows a clear factor-of-two reduction as  $B$  increases beyond  $\sim 30 \text{ mT}$ , which corresponds to  $B_\phi$  (Fig. 3b, uppermost panel). This suggests TRS to be preserved in GB regions at low  $n$ , similar to 2D systems such as exfoliated graphene [26], topological insulators [39], doped Si/Ge systems [40] and non-magnetic films [36]. However, with increasing  $n$ , a progressive reduction in  $\nu(B)$  at  $B = 0$  was observed across the GB approaching unity, and thus  $B$ -independent  $\nu$ , for  $n \gtrsim -6 \times 10^{12} \text{ cm}^{-2}$  (Fig. 3b, bottom panel). The insensitivity of  $\nu(B)$  to transverse field at the scale  $B \sim B_\phi$  is a unique characteristic of systems with spontaneously broken TRS, as observed before in ferromagnetic films [25] and lightly-doped semiconductors in strongly interacting regime [38]. A similar trend was observed for D2 (Figs. 3d, S5 and S6) where the reduction in  $\nu(B)$  was observed in both doping regimes. Remarkably, the spontaneous breaking of TRS was observed only in the inter-grain region, while the intra-grain region continues to show a factor-of-two reduction in UCF magnitude with  $B$  at similar high densities (Fig. 3c, higher  $T$  in Fig. S9). The near  $B$ -independence of  $\nu$  at high  $n$  was found to be ubiquitous to quantum transport across GBs in CVD graphene as shown for D1 in Fig. 3b and D2 in Fig. S5. The solid lines in Figs. 3b and c correspond to fits of  $\nu(B)$  according to Eq. 1 with  $l_\phi$  as the only fitting parameter. Fig. 3d shows the noise reduction factor  $\nu(B = 0) = N(B = 0)/N_\phi$  for D1 and D2 measured at  $T = 0.3$  and  $4.5 \text{ K}$  as a function of  $n$ . At  $T = 4.5 \text{ K}$ , the minimum  $\nu(B)$  ( $\approx 1.5$ ) at highest experimental  $n$  indicate only partial removal of TRS. The factor of two reduction of  $\nu(B)$  across the SG region was maintained throughout the entire density range, implying that TRS is lifted solely in the presence of the GB.

To understand the origin of TRS breaking in the GB region, we then measured the  $n$ -dependence of the zero- $B$  magnitude of UCF, which can distinguish between TRS breaking from external  $B$  field and that from an emergent frozen magnetic state [41]. For this,  $\langle \delta G_\phi^2 \rangle$  was calculated from reproducible fluctuations in  $G$  within small windows of  $V_{BG}$  i.e. from  $E_F$  (SM section S5). The SG region exhibits a factor of  $\approx 4$  reduction in  $\langle \delta G_\phi^2 \rangle$  (Fig. 4b, left panel) due to valley symmetry lifting thereby suppressing the UCF from valley triplet channels, a behaviour observed in exfoliated graphene [26]. In contrast, the UCF magnitude in the GB region ex-

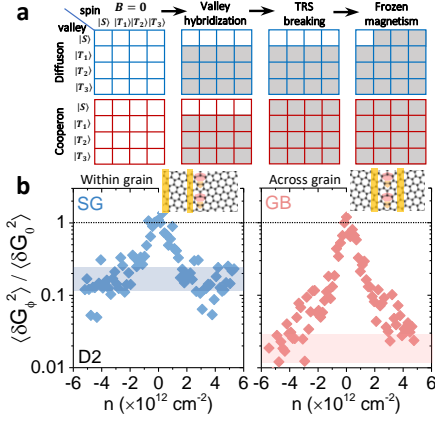


FIG. 4. **a**, Schematic describing the contribution of diffuson (blue) and cooperon (red) singlet ( $|S\rangle$ ) and triplet ( $|T_1\rangle$ ,  $|T_2\rangle$  and  $|T_3\rangle$ ) states to the UCF magnitude  $\langle \delta G_\phi^2 \rangle$  in different symmetry classes. Valley hybridization leads to a factor of four reduction in  $\langle \delta G_\phi^2 \rangle$  while magnetic impurities reduces  $\langle \delta G_\phi^2 \rangle$  by a further factor of eight due to gapping of spin diffuson triplets and all cooperons. **b**, The variance in conductance  $\langle \delta G_\phi^2 \rangle$  within a phase-coherent box of  $l_\phi^2$  normalized to its value at the Dirac point  $\delta \langle G_0^2 \rangle$  as a function of  $n$  at  $T = 0.3$  K, showing a factor of  $\approx 4$  reduction in the SG region and a factor of  $\approx 30$  reduction in the GB region.

hibits a drastic reduction (Fig. 4b, right panel) by a factor of  $\approx 30$  as  $n$  is increased. This unique and unprecedented reduction can be quantitatively understood from a combination of valley hybridization, TRS breaking and suppression of spin triplet channels in the presence of static (measurement time short compared to Korringa relaxation time) spin-dependent scattering, as depicted schematically in Fig. 4a. The static spin texture, or ‘frozen magnetic state’, at large  $n$  may happen when the defect-bound magnetic impurities interact via RKKY (Ruderman-Kittel-Kasuya-Yosida) exchange, forming long or short (*e.g.* a spin glass) range spin-ordered states [35, 42]. Thus, the UCF measurement in graphene containing a GB suggests a rather unexpected effect of doping, which manifests in both valley and (static) spin polarization when carrier density is made sufficiently large.

To estimate the energy scale for local moment interaction at the GB, we study the effect of temperature on  $\nu(B)$ . The normalized magnetonoise  $\nu(B)$  for the GB region in device D2 at  $n = 6.1 \times 10^{12} \text{ cm}^{-2}$  with varying temperature is shown in Fig. 5a (data at higher  $T$  in Fig. S7a). Evidently, the spontaneous TRS breaking occurs only at temperatures  $\lesssim 2$  K, while  $\nu(B)$  approaches  $\sim 2$  as  $T$  is increased (data for D2 at  $T = 4.5$  K in Fig. S6 and D3 at  $T = 8$  K in Fig. S8). To estimate the exchange interaction between moments, we first estimate the Kondo temperature  $T_K \simeq 20$  K from the  $T$ -dependence of the sheet resistance  $R_\square$  at finite  $B$  where WL corrections are suppressed (Fig. S14). This  $T_K$  is compatible with studies on irradiated graphene [3, 4].

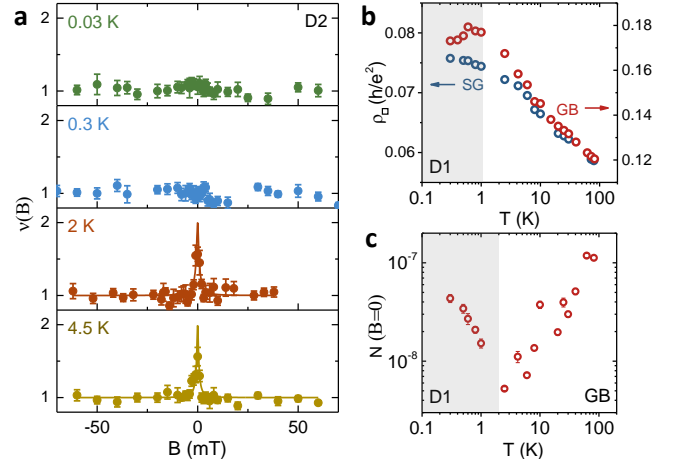


FIG. 5. **a**,  $\nu(B)$  plotted for D2 at  $n = 6.1 \times 10^{12} \text{ cm}^{-2}$  showing spontaneous TRS breaking at zero field only at temperatures  $T \lesssim 2$  K. **b**,  $T$ -dependence of the reduced sheet resistance  $\rho_\square$  (in units of  $h/e^2$ ) averaged from resistance fluctuations measurements at  $B = 0$  T for SG (blue) and GB (red) regions at  $n = -6 \times 10^{12} \text{ cm}^{-2}$  for D1. **c**, Normalized variance  $N = S_\sigma/\sigma^2$  at  $B = 0$  as a function of temperature is plotted for GB region of D1 at  $n = -6.9 \times 10^{12} \text{ cm}^{-2}$  clearly indicating a sharp increase in  $N(B = 0)$  at lower temperatures.

The RKKY interaction between moments can be estimated as [43]  $k_B T_{\text{RKKY}} \sim 27j^2 a^4 / 64\pi v_F \hbar R^3 \sim 2.2$  K (lattice constant  $a \approx 0.246$  nm and Fermi velocity in graphene  $v_F \approx 10^6$  m s $^{-1}$ ), where the Kondo exchange  $j \approx 2.3$  eV was obtained from the experimental  $T_K$  and the DOS in the GB region,  $D(E_F) \sim 0.05 \text{ eV}^{-1}$  (Fig. S12) [5–7]. Such a large  $j$  value agrees with previous theoretical calculations [44–46]. The average defect distance  $R \approx 2$  nm can be estimated from the HRTEM image of the GB region on alignment in two-beam condition (SM Fig. S13a with corresponding histogram in Fig. S13b). This value of  $T_{\text{RKKY}}$  agrees reasonably well with the  $T$  dependence of  $\nu(B = 0)$  (Fig. S7b), showing continual increase in  $\nu(B = 0)$  up to  $T \approx 10$  K, after which the decrease in  $\nu(B = 0)$  can be attributed to the loss of phase coherence through thermal averaging (Fig. S7a). The estimated values of  $T_K$  and  $T_{\text{RKKY}}$  signal a competition between Kondo singlet formation and a frozen magnetic state [47]. To gain further insight into the nature of this magnetic state, we have measured the time-averaged resistivity  $\rho_\square$  at  $n = -6 \times 10^{12} \text{ cm}^{-2}$  for the GB and SG regions of D1 simultaneously. A distinctive feature of the  $T$ -dependence of  $\rho_\square$  in the GB is a noticeable downturn at  $T \lesssim 1$  K (Fig. 5b), unlike the SG resistivity, despite accounting for quantum interference and  $e$ - $e$  interaction corrections. Such resistivity downturn at low- $T$  is strongly indicative of spin-glass freezing resulting from reduced spin-flip scattering [48, 49]. Additionally, the normalized variance  $N(B = 0)$  of the GB region increases rapidly by nearly an order of magnitude on cooling from  $\sim 2.5$  K to 0.3 K (Fig. 5c) despite the low- $T$  saturation in  $\gamma_{GB}$  (Fig. 2e), contrast-



ing with the behaviour of SG noise (Fig. S15). Such an anomalous increase cannot be explained by the standard Feng-Lee-Stone theory [37] but can be attributed to the chaotic nature of spin reorganization below the spin-glass freezing temperature [50], as previously reported in CuMn [51, 52], AuFe [53, 54] and dilute magnetic semiconductors [55].

In conclusion, we have identified signatures of spontaneous TRS breaking at graphene GBs using quantum transport measurements of WL and UCF. Such states emerge at high densities and at temperatures below  $\sim 2$  K suggesting low-energy spin-spin interactions, possibly mediated by RKKY coupling. An anomalously sharp increase in noise below  $\sim 2$  K indicates that the TRS breaking is likely due to an emergent spin glass state at graphene GBs.

---

\* These authors contributed equally to this work.;

<sup>5</sup> Present address: Materials Science Centre, Indian Institute of Technology Kharagpur, Kharagpur 721302, India;

<sup>6</sup> Present address: Department of Physics, Arizona State University, Tempe, AZ 85287, USA;

<sup>7</sup> Present address: Department of Metallurgical and Material Engineering, Indian Institute of Technology Kharagpur, Kharagpur 721302, India

- [1] M. M. Ugeda, I. Brihuega, F. Guinea, and J. M. Gómez-Rodríguez, Phys. Rev. Lett. **104**, 096804 (2010).
- [2] K. M. McCreary, A. G. Swartz, W. Han, J. Fabian, and R. K. Kawakami, Phys. Rev. Lett. **109**, 186604 (2012).
- [3] J.-H. Chen, L. Li, W. G. Cullen, E. D. Williams, and M. S. Fuhrer, Nat. Phys. **7**, 535 (2011).
- [4] Y. Jiang, P.-W. Lo, D. May, G. Li, G.-Y. Guo, F. B. Anders, T. Taniguchi, K. Watanabe, J. Mao, and E. Y. Andrei, Nat. Commun. **9** (2018).
- [5] L. Kou, C. Tang, W. Guo, and C. Chen, ACS Nano **5**, 1012 (2011).
- [6] S. S. Alexandre, A. D. Lúcio, A. H. Castro Neto, and R. W. Nunes, Nano Lett. **12**, 5097 (2012).
- [7] S. Dutta and K. Wakabayashi, Sci. Rep. **5**, 11744 (2015).
- [8] P. Nemes-Incze, P. Vancsó, Z. Osváth, G. I. Márk, X. Jin, Y.-S. Kim, C. Hwang, P. Lambin, C. Chapelier, and L. PéterBiró, Carbon **64**, 178 (2013).
- [9] A. Luican-Mayer, J. E. Barrios-Vargas, J. T. Falkenberg, G. Autès, A. W. Cummings, D. Soriano, G. Li, M. Brandbyge, O. V. Yazyev, S. Roche, and E. Y. Andrei, 2D Mater. **3**, 031005 (2016).
- [10] Q. Yu, L. A. Jauregui, W. Wu, R. Colby, J. Tian, Z. Su, H. Cao, Z. Liu, D. Pandey, D. Wei, T. F. Chung, P. Peng, N. P. Guisinger, E. A. Stach, J. Bao, S.-S. Pei, and Y. P. Chen, Nat. Mater. **10**, 443 (2011).
- [11] F. Gargiulo and O. V. Yazyev, Nano Lett. **14**, 250 (2013).
- [12] O. V. Yazyev and S. G. Louie, Nat. Mater. **9**, 806 (2010).
- [13] D. Van Tuan, J. Kotakoski, T. Louvet, F. Ortmann, J. C. Meyer, and S. Roche, Nano Lett. **13**, 1730 (2013).
- [14] J. C. Koepke, J. D. Wood, D. Estrada, Z.-Y. Ong, K. T. He, E. Pop, and J. W. Lyding, ACS Nano **7**, 75 (2013).
- [15] K. W. Clark, X.-G. Zhang, I. V. Vlassiouk, G. He, R. M. Feenstra, and A.-P. Li, ACS Nano **7**, 7956 (2013).
- [16] L. Tapasztó, P. Nemes-Incze, G. Dobrik, K. Jae Yoo, C. Hwang, and L. P. Biró, Appl. Phys. Lett. **100**, 053114 (2012).
- [17] L. A. Jauregui, H. Cao, W. Wu, Q. Yu, and Y. P. Chen, Solid State Commun. **151**, 1100 (2011).
- [18] A. W. Tsen, L. Brown, M. P. Levendorf, F. Ghahari, P. Y. Huang, R. W. Havener, C. S. Ruiz-Vargas, D. A. Muller, P. Kim, and J. Park, Science **336**, 1143 (2012).
- [19] V. Kochat, C. S. Tiwary, T. Biswas, G. Ramalingam, K. Hsieh, K. Chattopadhyay, S. Raghavan, M. Jain, and A. Ghosh, Nano Lett. **16**, 562 (2016).
- [20] J. Lahiri, Y. Lin, P. Bozkurt, I. I. Oleynik, and M. Batzill, Nat. Nanotechnol. **5**, 326 (2010).
- [21] P. Y. Huang, C. S. Ruiz-Vargas, A. M. van der Zande, W. S. Whitney, M. P. Levendorf, J. W. Kevek, S. Garg, J. S. Alden, C. J. Hustedt, Y. Zhu, J. Park, P. L. McEuen, and D. A. Muller, Nature **469**, 389 (2011).
- [22] J. Červenka, M. I. Katsnelson, and C. F. J. Flipse, Nat. Phys. **5**, 840 (2009).
- [23] C. W. J. Beenakker, Rev. Mod. Phys. **69**, 731 (1997).
- [24] A. D. Stone, Phys. Rev. B **39**, 10736 (1989).
- [25] S. Lee, A. Trionfi, and D. Natelson, Phys. Rev. B **70**, 212407 (2004).
- [26] A. N. Pal, V. Kochat, and A. Ghosh, Phys. Rev. Lett. **109**, 196601 (2012).
- [27] E. McCann, K. Kechedzhi, V. I. Fal'ko, H. Suzuura, T. Ando, and B. L. Al'tshuler, Phys. Rev. Lett. **97**, 146805 (2006).
- [28] F. Pierre, H. Pothier, D. Esteève, M. H. Devoret, A. B. Gougam, and N. O. Birge, in *Kondo effect and dephasing in low-dimensional metallic systems*, edited by V. Chandrasekhar, C. Van Haesendonck, and A. Zawadowski (Kluwer, Dordrecht, 2001) pp. 119–132.
- [29] F. Pierre and N. O. Birge, Phys. Rev. Lett. **89**, 206804 (2002).
- [30] F. Pierre, A. B. Gougam, A. Anthore, H. Pothier, D. Esteve, and N. O. Birge, Phys. Rev. B **68**, 085413 (2003).
- [31] S. V. Morozov, K. S. Novoselov, M. I. Katsnelson, F. Schedin, D. C. Elias, J. A. Jaszczak, and A. K. Geim, Phys. Rev. Lett. **100**, 016602 (2008).
- [32] F. V. Tikhonenko, A. A. Kozikov, A. K. Savchenko, and R. V. Gorbachev, Phys. Rev. Lett. **103**, 226801 (2009).
- [33] M. B. Maple, in *Magnetism Volume V: Magnetic Properties of Magnetic Alloys*, edited by H. Suhl (Academic Press, New York, 1973) p. 289.
- [34] C. V. Haesendonck, J. Vranken, and Y. Bruynseraede, Phys. Rev. Lett. **58**, 1968 (1987).
- [35] F. Schopfer, C. Bäuerle, W. Rabaud, and L. Saminadayar, Phys. Rev. Lett. **90**, 056801 (2003).
- [36] N. O. Birge, B. Golding, and W. H. Haemmerle, Phys. Rev. B **42**, 2735 (1990).
- [37] S. Feng, P. A. Lee, and A. D. Stone, Phys. Rev. Lett. **56**, 1960 (1986).
- [38] S. Shamim, S. Mahapatra, G. Scappucci, W. M. Klesse, M. Y. Simmons, and A. Ghosh, Phys. Rev. Lett. **112**, 236602 (2014).
- [39] S. Islam, S. Bhattacharyya, H. Nhalil, S. Elizabeth, and A. Ghosh, Phys. Rev. B **97**, 241412(R) (2018).
- [40] S. Shamim, S. Mahapatra, G. Scappucci, W. Klesse, M. Simmons, and A. Ghosh, Sci. Rep. **7**, 46670 (2017).
- [41] E. Akkermans and G. Montambaux, *Mesoscopic Physics of Electrons and Photons* (Cambridge University Press,

- 2007).
- [42] P. W. Anderson, in *Les Houches, Ill-condensed matter, Session XXXI*, edited by R. Balian, R. Maynard, and G. Toulouse (Amsterdam: North Holland, 1978) pp. 159–261.
  - [43] M. Sherafati and S. Satpathy, Phys. Rev. B **83**, 165425 (2011).
  - [44] K. Sengupta and G. Baskaran, Phys. Rev. B **77**, 045417 (2008).
  - [45] M. A. Cazalilla, A. Iucci, F. Guinea, and A. H. Castro Neto, arXiv preprint arXiv:1207.3135 (2012).
  - [46] A. K. Mitchell and L. Fritz, Phys. Rev. B **88**, 075104 (2013).
  - [47] S. Doniach, Physica B+C **91**, 231 (1977).
  - [48] G. Neuttiens, J. Eom, C. Strunk, V. Chandrasekhar, C. V. Haesendonck, and Y. Bruynseraede, EPL (Europhys. Lett.) **34**, 617 (1996).
  - [49] G. Forestier, M. Solana, C. Naud, A. D. Wieck, F. m. c. Lefloch, R. Whitney, D. Carpentier, L. P. Lévy, and L. Saminadayar, Phys. Rev. B **102**, 024206 (2020).
  - [50] S. Feng, A. J. Bray, P. A. Lee, and M. A. Moore, Phys. Rev. B **36**, 5624 (1987).
  - [51] N. E. Israeloff, M. B. Weissman, G. J. Nieuwenhuys, and J. Kosiorowska, Phys. Rev. Lett. **63**, 794 (1989).
  - [52] P. W. Fenimore and M. B. Weissman, J. Appl. Phys. **85**, 8317 (1999).
  - [53] K. A. Meyer and M. B. Weissman, Phys. Rev. B **51**, 8221 (1995).
  - [54] G. Neuttiens, C. Strunk, C. Van Haesendonck, and Y. Bruynseraede, Phys. Rev. B **62**, 3905 (2000).
  - [55] J. Jaroszyński, J. Wróbel, G. Karczewski, T. Wojtowicz, and T. Dietl, Phys. Rev. Lett. **80**, 5635 (1998).

**Acknowledgements** We are grateful to H. R. Krishnamurthy, Sumilan Banerjee and Sudipta Dutta for useful discussions. K.H., V.K. and A.G acknowledge the Department of Science and Technology (DST) for a funded project. K.H. and A.G. also thank the National Nanofabrication Center, CeNSE, IISc (NNfC) for providing clean room facilities.

# Spontaneous time reversal symmetry breaking at individual grain boundaries in graphene: (Supplemental Material)

Kimberly Hsieh<sup>1,a,b</sup>, Vidya Kochat<sup>1,5,a</sup>, Tathagata Biswas<sup>1,6</sup>, Chandra Sekhar Tiwary<sup>2,7</sup>, Abhishek Mishra<sup>3</sup>, Gopalakrishnan Ramalingam<sup>4</sup>, Aditya Jayaraman<sup>1</sup>, Kamanio Chattopadhyay<sup>2</sup>, Srinivasan Raghavan<sup>3,4</sup>, Manish Jain<sup>1</sup> & Arindam Ghosh<sup>1,3</sup>

<sup>1</sup> *Department of Physics, Indian Institute of Science, Bangalore 560 012, India*

<sup>2</sup> *Department of Materials Engineering,  
Indian Institute of Science, Bangalore 560 012, India*

<sup>3</sup> *Centre for Nano Science and Engineering,  
Indian Institute of Science, Bangalore 560 012, India*

<sup>4</sup> *Materials Research Center, Indian Institute of Science, Bangalore 560 012, India*

<sup>5</sup> *Present address: Materials Science Centre,  
Indian Institute of Technology Kharagpur, Kharagpur 721302, India*

<sup>6</sup> *Present address: Department of Physics,  
Arizona State University, Tempe, AZ 85287, USA and*

<sup>7</sup> *Present address: Department of Metallurgical and Material Engineering,  
Indian Institute of Technology Kharagpur, Kharagpur 721302, India*

---

<sup>a</sup> equal contributions

<sup>b</sup> email: kimberly@iisc.ac.in

## S1. Methods

### 1. Graphene growth and device fabrication

Graphene grains are grown by low pressure chemical vapour deposition (CVD) on Alfa Aesar ( $25\text{ }\mu\text{m}$ ) Cu foils. The Cu foil is wrapped to form an enclosure, and placed inside a 1 inch quartz tube reaction chamber. Initially, 100 SCCM of  $\text{H}_2$  gas was passed through the reaction chamber for flushing out impurities from the Cu surface and subsequently, the Cu foil was annealed at  $1000^\circ\text{C}$  for 4 hours while the flow rate was reduced to 50 SCCM of  $\text{H}_2$ . A mixture of  $\text{CH}_4$ ,  $\text{H}_2$  and  $\text{N}_2$  gases in the ratio of 5:500:1000 was passed for  $\sim 30$  seconds following which, the furnace was cooled to room temperature under a constant flow rate of 50 SCCM of  $\text{H}_2$ . The Cu foil with graphene was then spin-coated with polymethyl methacrylate (MicroChem PMMA 950K) at 2000 RPM and allowed to dry at room temperature. The polymer-graphene-Cu foil stack was then suspended in 0.1 M ammonium persulphate solution to etch the Cu foil. The floating PMMA-graphene stack was rinsed thoroughly with DI water and transferred onto clean Si/ $\text{SiO}_2$  (285 nm) substrates by dissolving the PMMA using hot acetone. Suitable pairs of graphene grains were chosen and patterned by electron beam lithography followed by metallization of the contacts.

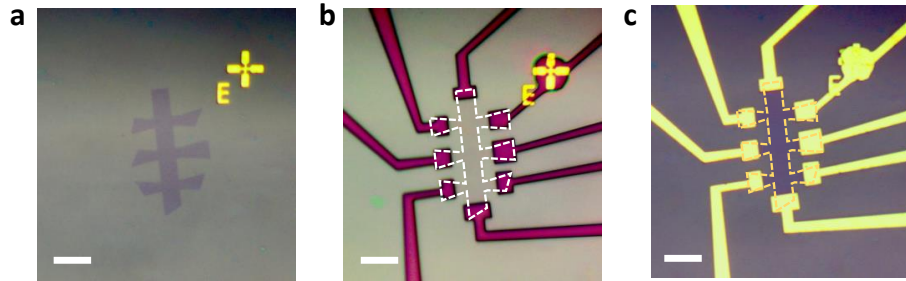


Figure S1. **Optical microscope images of the device at various stages of fabrication.** **a** Selected pair of CVD graphene grains etched into Hall bar geometry using reactive ion etching with  $\text{O}_2$  plasma. **b** Electrical contacts defined by e-beam lithography. **c** Final image of the device after metallization. Scale bar,  $10\text{ }\mu\text{m}$ .



## 2. Transport measurements

Magnetotransport measurements were either carried out in a Janis He-3-SSV refrigerator (for  $0.3 \text{ K} \leq T \leq 40 \text{ K}$ ) or a Leiden MNK-126  $^3\text{He}/^4\text{He}$  dilution refrigerator (for  $0.03 \text{ K} \leq T \leq 5 \text{ K}$ ). Both time-dependent and gate voltage-dependent conductance fluctuations measurements were obtained using low-frequency lock-in method. The gate voltage-dependent UCF was measured using two-probe resistance configuration [1] where successive but overlapping windows of 4 V interval were chosen such that the conductance does not change appreciably but significant fluctuations were present for a statistically meaningful analysis ( $\sim 800$  realizations). For time-dependent conductance fluctuations, an AC four-probe Wheatstone bridge configuration was used to measure the fluctuations in resistance at a fixed  $n$ . The time series data was digitized and decimated in multiple stages to obtain the power spectral density (PSD), which was then integrated over the experimental bandwidth to obtain the normalized variance  $N = \int \frac{S_G}{G^2} df = \frac{\langle G^2 \rangle}{G^2}$  (Fig. S3a). Care was taken to minimize heating of the electrons by ensuring that the source-drain bias  $V_{\text{SD}} \lesssim k_{\text{B}}T/e$ .

## 3. DFT calculations

All first principles calculations have been performed within the framework of SIESTA [2] code. We use norm-conserving pseudopotentials [3] and Generalized Gradient approximation [4] (PBE) for exchange correlation functional. A double- $\zeta$  plus polarization (DZP) basis set and a mesh cut-off of 300 Ry have been chosen for Brillouin zone integrations. For the calculations of both GB(2,0)|(2,0) and GB(5,0)|(3,3),  $1 \times 10 \times 50$  k-grid have been employed. All the atomic positions are relaxed using conjugate-gradient algorithm until the forces were less than  $0.04 \text{ eV}/\text{\AA}$ .

## S2. Weak localization measurements for D1 at $T = 0.3$ K

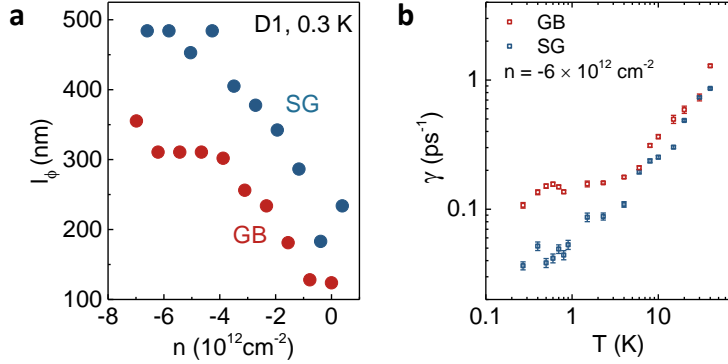


Figure S2. **a**, The  $l_\phi$  values at 0.3 K obtained from the magnetoresistance fitting for graphene is plotted for the SG and GB regions as a function of  $n$ . **b**, The scattering rates  $\gamma$  (obtained from the HLN fits to the magnetoconductance data) plotted as a function of temperature  $T$  for the SG and GB regions at  $n = -6 \times 10^{12} \text{ cm}^{-2}$ .

## S3. Noise for D1 at $B = 0$ T

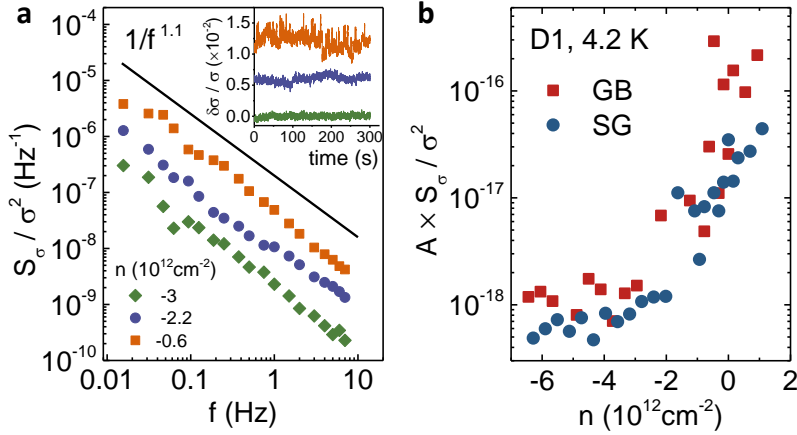


Figure S3. **1/f noise for D1 at zero magnetic field.** **a**, The normalized power spectrum for D1 at  $T = 4.2$  K is plotted for three different  $n$  showing clear  $1/f$  behaviour. The inset shows the conductivity fluctuations for these  $n$  clearly showing that the fluctuation magnitude is increased at low  $n$ . **b**, The area-normalized power spectral density ( $A \times S_v / \sigma^2$ ) is shown for the SG and GB regions of D1 as a function of  $n$  at  $T = 4.2$  K.

The time-dependent conductance fluctuations in the inter-grain region measured at different carrier densities is shown in the inset of Fig. S3a. The power spectrum obtained from these conductivity fluctuations exhibit  $1/f$  behaviour in the frequency domain as shown in Fig. S3a. The area-normalized power spectrum ( $A \times S_\sigma/\sigma^2$ ) as a function of  $n$  at 4.2 K is shown in Fig. S3b for the SG and GB regions. The noise in the GB region is larger than the SG region indicating more dynamic scattering arising from the localized states at the GBs [5].

#### S4. UCF from time-dependent conductance fluctuations

For time-dependent conductance fluctuations, an AC four-probe Wheatstone bridge configuration was used to measure the fluctuations in resistance at a fixed  $n$  and a fixed  $B$ . Two resistors,  $R1$  and  $R2$  form the upper arms of the Wheatstone's bridge.  $R1 \sim 1 \text{ M}\Omega$  is the current limiting resistor through which the sample is biased using an AC voltage from the lock-in amplifier (SR830). The variable resistor  $R3$  in the third arm is designed using a series of low drift  $1 \text{ k}\Omega$ ,  $10 \text{ k}\Omega$  and  $100 \text{ k}\Omega$  potentiometers. For each  $B$  at a fixed  $V_{BG}$ , the bridge is balanced by varying  $R3$  and the small unbalanced voltage is first amplified using the SR560 preamplifier with a chosen gain of 100 and then measured in the A-B mode of the lock-in amplifier with a high sensitivity, with the B port connected to ground via a  $50 \text{ }\Omega$  terminator. The entire setup is shielded using a grounded Faraday cage to minimize electromagnetic interference. The signal from both the in-phase (X) and quadrature (Y) channels of the lock-in amplifier are digitized at a high sampling frequency  $f_s$  (1000 samples per second) using a 16-bit ADCs (analog-to-digital converters) NI USB-6210 from National Instruments with a maximum sampling rate of 250 Kilosamples per second, 4095 samples of on-board memory and an input impedance of  $\sim 10 \text{ G}\Omega$ , which can be interfaced with LabVIEW programs. The data is stored in the on-board memory temporarily and then transferred to the hard disk of the computer in segments for further processing.

The time series data was then decimated in multiple stages to obtain the power spectral density (PSD) using the fast Fourier transform (FFT) technique, which was then integrated over the experimental bandwidth to obtain the normalized variance  $N = \int \frac{S_G}{G^2} df = \frac{\langle G^2 \rangle}{G^2}$  at each  $B$  for a fixed  $V_{BG}$ . Care was taken to minimize heating of the electrons by ensuring that the source-drain bias  $V_{SD} \lesssim k_B T/e$ . More details of the experimental technique can be found in Ref. [6]. The evaluation of the variance  $\langle \delta G_\phi^2 \rangle$  was obtained from statistically

meaningful windows of time ( $\approx 1200$  seconds with  $\approx 18750$  realizations of  $G$ ).

### S5. UCF from gate voltage-dependent conductance fluctuations

UCF measurements were performed in D2 using the two-probe resistance configuration [1]. The phase coherence length ( $l_\phi$ ) was extracted from the WL MC curves using the modified Hikami-Larkin-Nagaoka expression [7]. Successive gate voltage windows of 4 V interval were chosen such that the conductance does not change appreciably but significant fluctuations are nevertheless present for a statistically meaningful analysis ( $\sim 800$  realizations). This

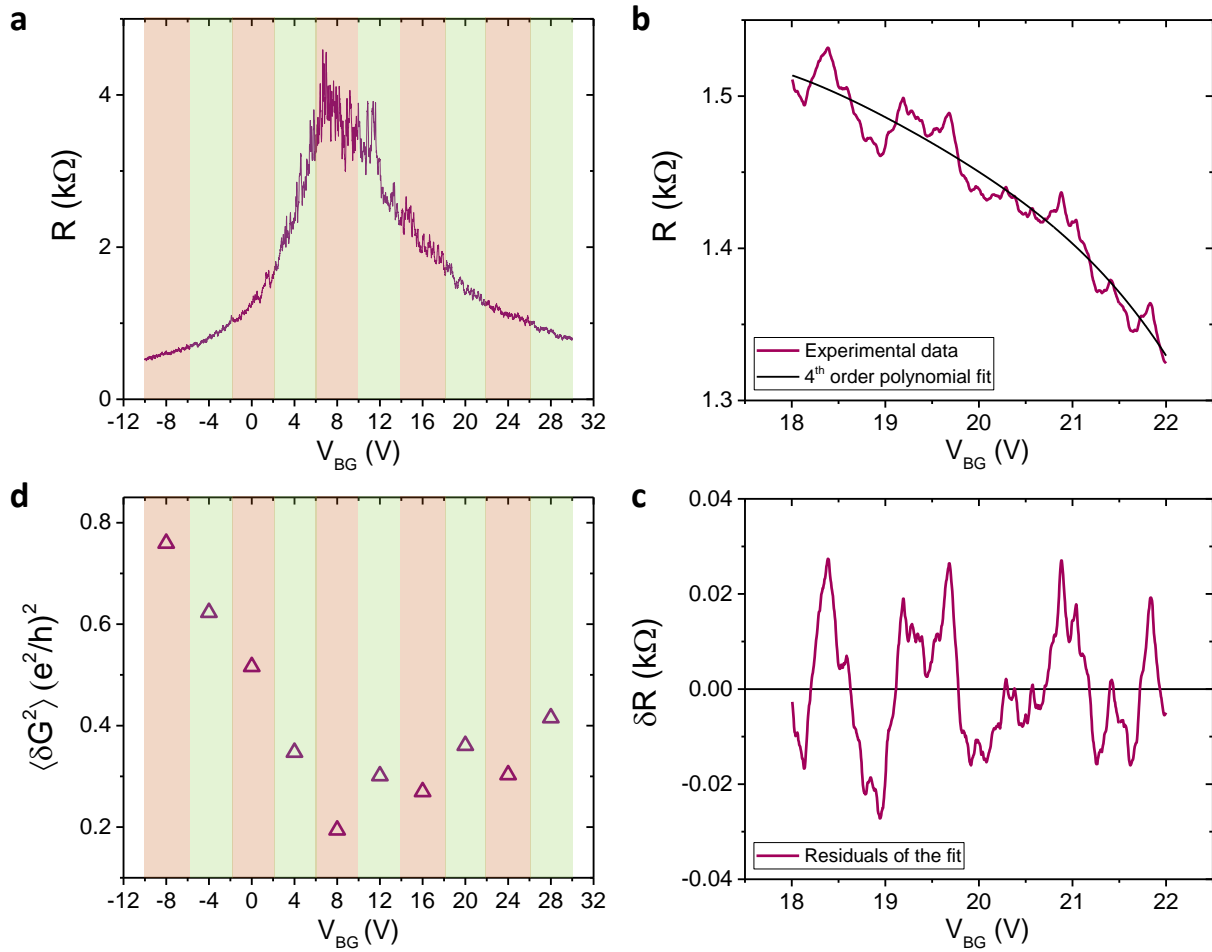


Figure S4. **a**, A typical plot of two-probe resistance as a function of back gate voltage for graphene, split into successive 4 V interval windows. **b**, The resistance fluctuations within a 4 V window range plotted along with its fourth order polynomial fit. **c** The residuals obtained from the fourth order polynomial fit of the curve in **b**. **d** The calculated values of  $\langle \delta G^2 \rangle$  corresponding to the different gate voltage windows of the representative curve in **a**.

is demonstrated in Fig. S4a for a typical transfer characteristic curve of graphene. The two-probe resistance in each  $V_{\text{BG}}$  window was then fitted with a fourth-order polynomial as shown in Fig. S4b, and then the variance of the fluctuations was calculated from the residuals of the fit as shown in Fig. S4c. The fitting with a fourth-order polynomial was done to subtract a smooth background for calculating the fluctuations and to suppress slowly varying changes in the conductance. Fitting with polynomials of other orders do not give any qualitative difference in the analysis [8, 9]. Finally, the magnitude of conductance fluctuations is obtained from the resistance fluctuations as

$$\langle \delta G^2 \rangle = \frac{\langle \delta R^2 \rangle}{\langle R \rangle^4} \quad (1)$$

where  $\langle R \rangle$  is the average four-terminal resistance corresponding to that particular gate voltage window. However, this measured  $\langle \delta G^2 \rangle$  arises from the entire sample and in order to obtain the magnitude of conductance fluctuations within a phase-coherent box of area  $l_\phi \times l_\phi$ , the principle of superposition is invoked which gives

$$\frac{\langle \delta G^2 \rangle}{\langle G \rangle^2} = \frac{1}{N} \frac{\langle \delta G_\phi^2 \rangle}{\langle G_\phi \rangle^2} \quad (2)$$

where  $N = LW/l_\phi^2$  is the number of phase coherent boxes within the channel of length  $L$  and width  $W$ . Since  $\langle \delta G_\phi^2 \rangle = \sigma$  and  $\langle \delta G^2 \rangle = \sigma W/L$ ,

$$\langle \delta G_\phi^2 \rangle = \frac{L^3}{W} \frac{\langle \delta G^2 \rangle}{l_\phi^2} \quad (3)$$

Both the phase breaking length ( $l_\phi$ ) and the variance of conductance fluctuations ( $\langle \delta G^2 \rangle$ ) are dependent on carrier density and have to be evaluated experimentally to extract the density dependence of  $\langle \delta G_\phi^2 \rangle$ .

## S6. Magneto-noise data for devices D2 and D3

### 1. D2 at $T = 0.3$ K

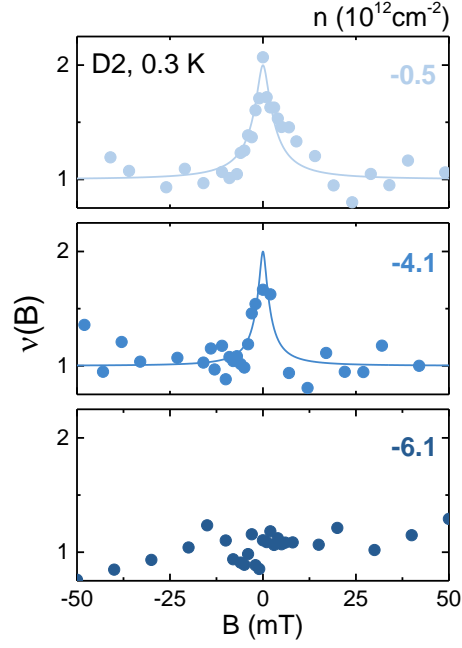


Figure S5.  $\nu(B)$  for D2 at  $T = 0.3$  K for different carrier densities  $n$  in units of  $10^{12} \text{ cm}^{-2}$ . Solid lines are fits to the crossover function.



## 2. D2 at $T = 4.5$ K

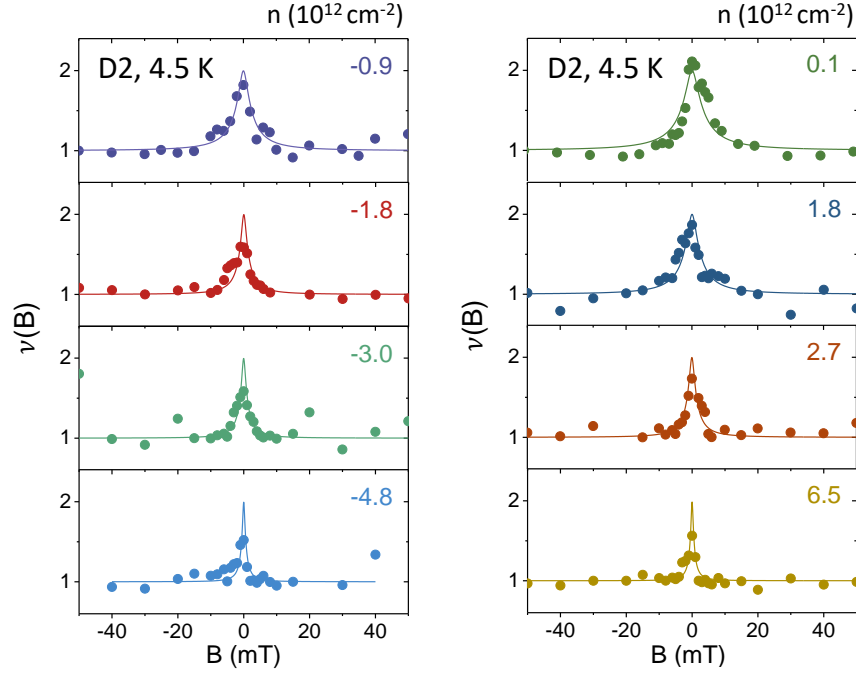


Figure S6.  $\nu(B)$  for D2 at  $T = 4.5$  K for different carrier densities  $n$  in units of  $10^{12} \text{ cm}^{-2}$ . Solid lines are fits to the crossover function.

### 3. D2 at higher $T$

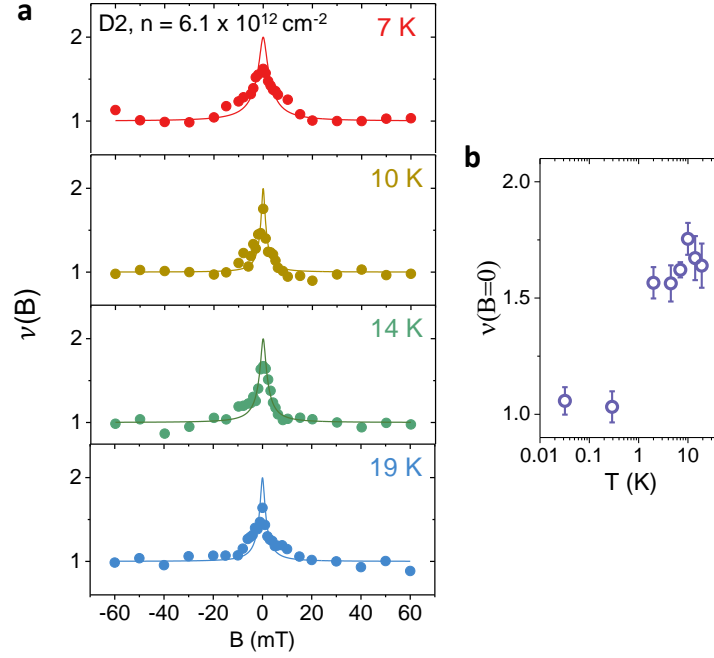


Figure S7. **a**,  $\nu(B)$  for GB of D2 at  $T = 7, 10, 14$  and  $19$  K for  $n = 6.1 \times 10^{12} \text{ cm}^{-2}$ . Solid lines are fits to the crossover function. **b**, The reduction factor  $\nu(B = 0)$  of the time-dependent UCF in the intergrain region plotted as a function of temperature  $T$  at high electron density  $n = 6.1 \times 10^{12} \text{ cm}^{-2}$ .

From Fig. S7, we observe that the spontaneous TRS breaking in graphene GBs happens only at ultra-low temperatures below  $\sim 1 - 2$  K.  $\nu(B = 0)$  continues to increase as  $T$  increases up to  $\approx 10$  K, after which  $\nu(B = 0)$  starts to decrease as quantum interference effects begin to disappear due to loss of phase coherence. At higher temperatures, the  $1/f$  noise can no longer be attributed entirely to UCF [10].

#### 4. D3 at $T = 8$ K

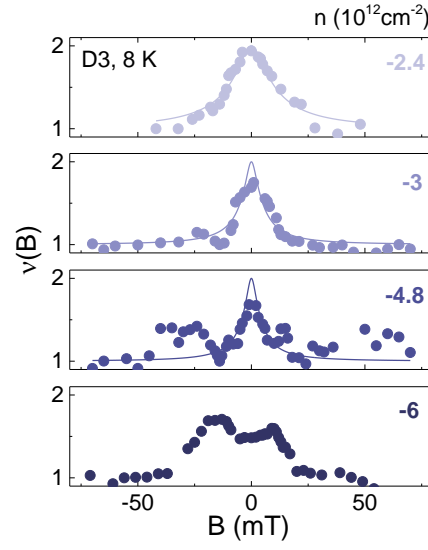


Figure S8.  $\nu(B)$  for D3 at  $T = 8$  K for different carrier densities  $n$  in units of  $10^{12} \text{ cm}^{-2}$ . Solid lines are fits to the crossover function.

### 5. Single grain magneto-noise for D2 at $T = 4.5$ K

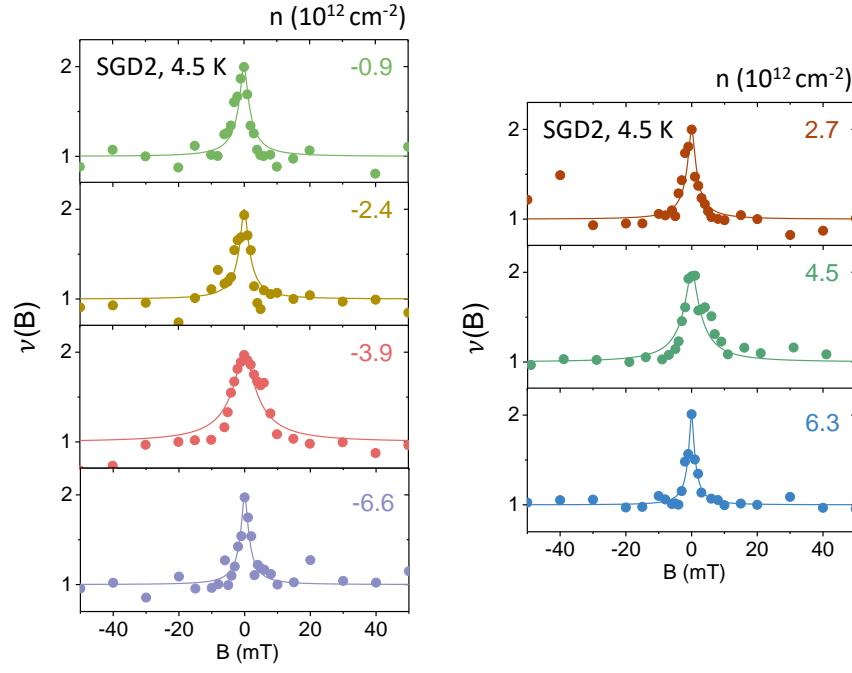


Figure S9.  $\nu(B)$  for the single grain region (without GB) of D2 at  $T = 4.5$  K for different carrier densities  $n$  in units of  $10^{12} \text{ cm}^{-2}$ , showing factor-of-two reduction in the magneto-noise even at high  $n$  unlike the case of the inter-grain region. Solid lines are fits to the crossover function.

## S7. Density functional calculations for atomically sharp grain boundaries

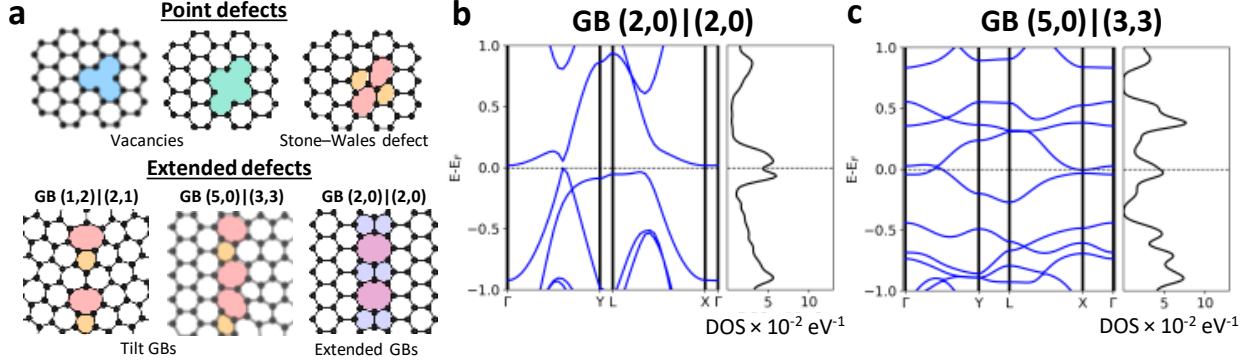


Figure S10. **a**, Schematic showing two categories of defects in graphene: point and extended defects. **b,c**, Bandstructure and density of states calculations for graphene with GB containing **b**, pentagon-octagon defects (GB(2,0)|(2,0)) and **c**, pentagon-heptagon defects (GB(5,0)|(3,3)) showing enhanced DOS due to flat band formation.

## S8. Density functional calculations for a grain boundary of finite width

GB(6,6)|(6,6) can be thought of as a clean translational GB(2,0)|(2,0) sandwiched between two GB(3,3)|(5,0), type of GBs [11]. GB(3,3)|(5,0) consists of only Stone-Wales 5-7 defects while GB(2,0)|(2,0) contains only 5-8 defect pairs. To match the periodicity in the direction parallel to the GB, five unit cells of GB(2,0)|(2,0) and two unit cells of GB(3,3)|(5,0) were used resulting in a matching vector (10,0) in region between the two GBs and (6,6) in the region beyond either GB(3,3)|(5,0). For the calculations of GB(2,0)|(2,0),  $1 \times 10 \times 50$  k-grid was employed. However, for the newly proposed GB(6,6)|(6,6), the number of k-points along the z-direction was reduced by a factor of 5 due to the larger supercell size. The calculations were carried out on a supercell of 242 atoms where the separation between two adjacent GBs in GB(6,6)|(6,6) was fixed at  $\sim 10 \text{ \AA}$ .

Fig. S11a shows the band structure of GB(2,0)|(2,0) for three cases of zero-, hole- and electron-doping. The ferromagnetic state arises only for the case of electron doping as the Fermi level is raised due to Stoner instability. The localized core states in the GB regions give rise to flat bands near the Fermi level which split near the  $\Gamma$ -point resulting in a non-zero magnetic moment. On the other hand, the band structure and density of state (DOS) plots for GB(6,6)|(6,6) show spin-splitting not only near the  $\Gamma$ -point but throughout the

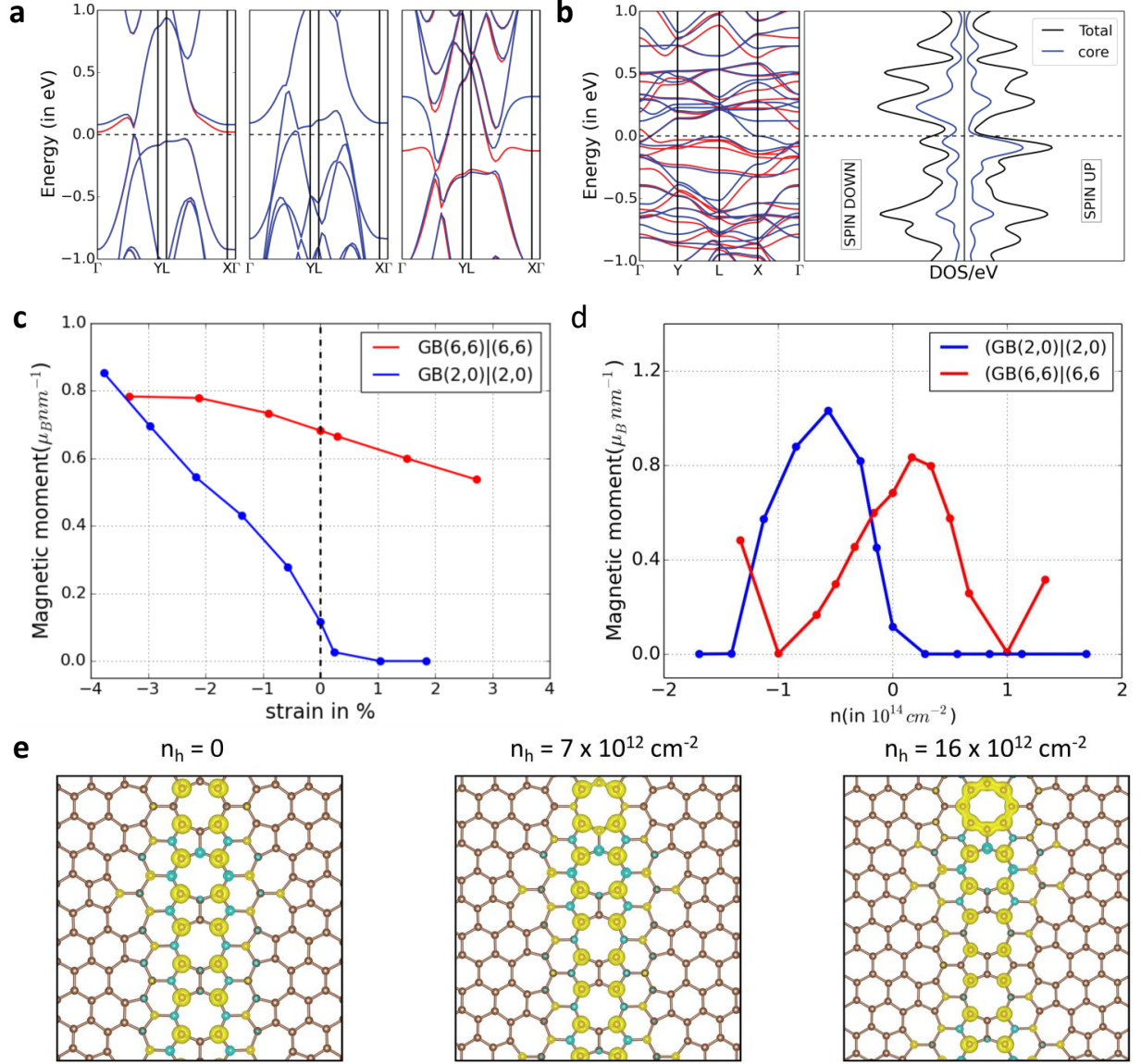


Figure S11. **a**, Band structure of GB(2,0)|(2,0) where the three panels represent zero doping, hole doping of  $-5.6 \times 10^{13} \text{ cm}^{-2}$  and electron doping of  $5.6 \times 10^{13} \text{ cm}^{-2}$  respectively. **b**, Left panel shows the band structure of and spin polarized density of states (DOS) for GB(6,6)|(6,6). Right panel shows the projected DOS for only the core atoms. **c,d**, Magnetic moment per unit length of the GB for both GB(2,0)|(2,0) and GB(6,6)|(6,6) as a function of **c** uniaxial strain along the armchair direction and **d** carrier density  $n$ . **e** Isosurface showing the spin polarization density along the GB(6,6)|(6,6) at different densities of hole doping.

entire Brillouin zone. The origin of the magnetic moments may be attributed to the in-built lattice strain due to the additional 5-7 defects around the GB region. It is important to note



that  $\text{GB}(6,6)|(6,6)$  has a lattice dimension five times larger than that of  $\text{GB}(2,0)|(2,0)$  in the Y-direction, hence it is necessary to take zone folding into account while comparing the band structures of the two GBs. The additional flat bands near the Fermi level may come directly from the random distribution of Stone-Wales defects or via internal strain due to their presence. The spin-split bands are not only spread throughout the Brillouin zone but also across an energy range. The bands are split in the range of 1 eV above and below the Fermi level, which explains the dependence of the magnetic moment per unit length as a function of changing carrier density (Fig. S11d). The doping response can also be explained from the spin polarized DOS plots for  $\text{GB}(6,6)|(6,6)$  shown in the right panel of Fig. S11b. The core atoms consist of the 5-8 defects which host almost all the magnetic moments as seen in the isosurface plots of Fig. S11e.

Consistent with the findings of previous theoretical studies [11–13], 5-8 defects of translational  $\text{GB}(2,0)|(2,0)$  were found to host a ferromagnetic ground state when the system is doped [11] or strained [12]. Our theoretical calculations show that application of a tensile strain along the zigzag direction or compressive strain along the armchair direction significantly enhances the magnetic moment per unit length along the GB (Fig. S11c). The strain is believed to arise during the growth and subsequent transfer process of the graphene grains on to  $\text{SiO}_2$  substrate. Fig. S11c also reveals a striking difference between the two GBs.  $\text{GB}(6,6)|(6,6)$  exhibits a significantly large magnetic moment even in the absence of external strain. The response to an external strain along the armchair direction is much lesser for  $\text{GB}(6,6)|(6,6)$  as compared to  $\text{GB}(2,0)|(2,0)$  since the additional 5-7 defects around the core 5-8 defects in  $\text{GB}(6,6)|(6,6)$  are expected to absorb a significant fraction of the strain applied.

The variation of magnetic moments as a function of carrier density  $n$  is plotted in Fig. S11d. For  $\text{GB}(2,0)|(2,0)$ , electron doping induces significant magnetic moment formation which diminishes once the doping density is increased above  $\sim -0.5 \times 10^{14} \text{ cm}^{-2}$ , far beyond the range accessible by an  $\text{SiO}_2$  back gate. This can be explained from the sharp resonance in the DOS located at about  $\pm 0.1$  eV of the Fermi level, which consists of the localized core states in the GB region. The magnetic moments originate from the Coulomb interaction between the electrons in these states [11]. In addition to the fact that there is a significantly large magnetic moment formation at zero doping for  $\text{GB}(6,6)|(6,6)$ , the response to doping is also very different from that of  $\text{GB}(2,0)|(2,0)$ . The magnetic moments

are formed for both hole and electron doping unlike the case of  $\text{GB}(2,0)|(2,0)$  as explained earlier from the band structure and DOS shown in Fig. S11a. The isosurface of spin polarization density is showing for  $\text{GB}(6,6)|(6,6)$  in Fig. S11e for the undoped system as well as two different hole doping densities. The spin polarization value was chosen as  $1.5 \times 10^{-3} \mu_B$  for plotting these isosurfaces. For the undoped system, the magnetic moments are localized on the atoms along the zigzag edges in the middle of the GB, consistent with the case of  $\text{GB}(2,0)|(2,0)$  [11, 12]. As the number density is tuned, the C-C dimer connecting the two zigzag edges begin to host magnetic moments as well. On increasing the hole density further, some of the atoms of the different sublattice of the zigzag edge reverse their spin polarizations which leads to a net enhancement of the overall magnetic moment of the GB. These moments may explain the spontaneous breaking of time reversal symmetry at higher densities, if they interact to result in a frozen magnetic order.

### S9. DOS per site for different types of GBs

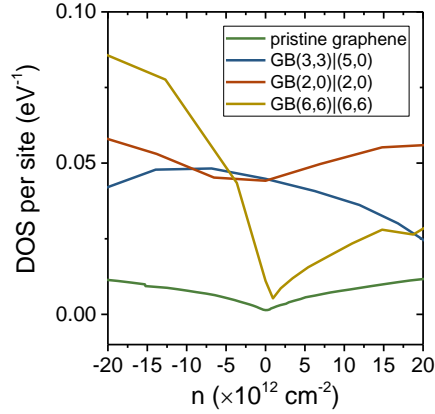


Figure S12. DOS per site as a function of  $n$  for pristine graphene (green),  $\text{GB}(3,3)|(5,0)$  with only pentagon-heptagon defects (blue),  $\text{GB}(2,0)|(2,0)$  with only pentagon-octagon defects (red) and finite width  $\text{GB}(6,6)|(6,6)$  with multiple types of defects (yellow).

### S10. Mapping the defect disorder in a grain boundary of finite width

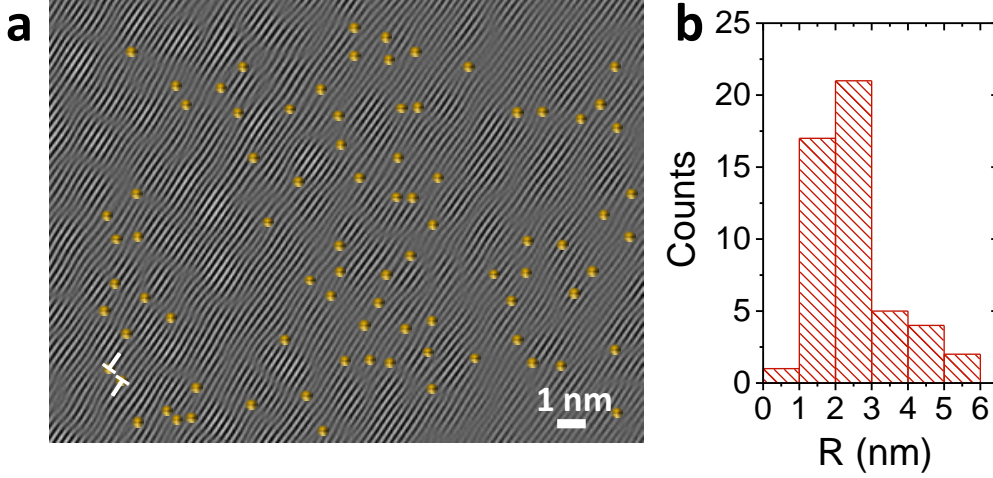


Figure S13. **a**, Experimental demonstration of defect-induced distortion on the parallel lattice array of a representative HRTEM image of a finite-width GB. **b**, Histogram obtained from the HRTEM image in **a** revealing an average defect distance  $R \approx 2$  nm.

### S11. Estimation of Kondo temperature $T_K$

The Kondo temperature  $T_K$  can be extracted from the temperature dependence of the reduced sheet resistance  $\rho_{\square}$  ( $R_{\square}$  in units of  $h/e^2$ ) at  $B = 0.5$  T where weak localization effects have been mostly eliminated. Assuming contributions only from a  $T$ -independent longitudinal resistivity  $\rho_c$ , electron-electron scattering-induced correction  $\rho_{e-e}$  [14, 15] and a Kondo contribution  $\rho_K$  [16, 17]:

$$\begin{aligned} \rho_{\square} &= \rho_c + \rho_{e-e} + \rho_K \\ &= \rho_c + (\mu^2 B^2 - 1) \frac{\rho_c^2}{\pi} A \ln \frac{\hbar}{k_B T \tau_{tr}} + \rho_{K,0} \left[ 1 + \left( \frac{T}{T_K} \right)^2 (2^{1/0.22} - 1) \right]^{-0.22} \end{aligned} \quad (4)$$

where  $\mu$  is the device mobility, the coefficient  $A = 1 + c \left[ 1 - \frac{\ln(1+F_0^\sigma)}{F_0^\sigma} \right]$  is a measure of the interaction strength (where  $F_0^\sigma$  is the Fermi-liquid constant and  $c$  is the number of contributing multiplet channels),  $\tau_{tr}$  is the transport time derived from the Drude resistivity, and  $\rho_K$  is the Kondo resistivity at zero temperature. Fig. S14a show the fits to Eq. 4 for the resistivity versus temperature data of the SG (blue circles) and GB (red circles) regions

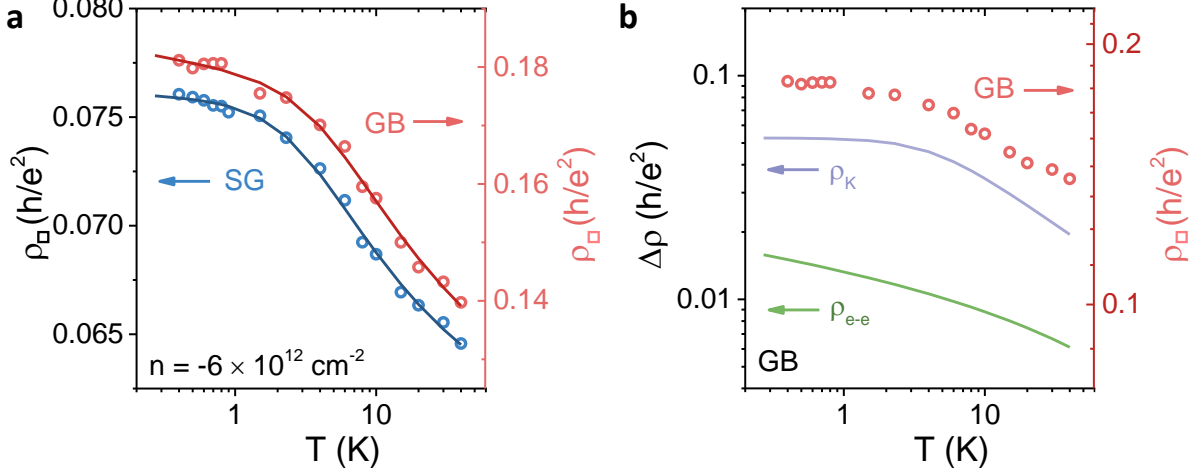


Figure S14. **a**,  $T$ -dependence of the reduced sheet resistance  $\rho_{\square}$  (in units of  $h/e^2$ ) measured at  $B = 0.5$  T for the SG region (blue circles) and the GB region (red circles) at  $n = -6 \times 10^{12} \text{ cm}^{-2}$ . The solid lines show fit to the Eq. 4, which includes electron-electron interaction corrections  $\rho_{e-e}$  and the Kondo contribution to resistivity  $\rho_K$ . **b**, The extracted values of  $\rho_{e-e}$  (green solid line),  $\rho_K$  (purple solid line) and the experimentally obtained  $\rho_{\square}$  for the GB region at  $n = -6 \times 10^{12} \text{ cm}^{-2}$  are plotted as a function of  $T$  to show their relative magnitudes.

at  $n = -6 \times 10^{12} \text{ cm}^{-2}$ , keeping  $\rho_c$ ,  $\rho_{K,0}$ ,  $A$  and  $T_K$  as fitting parameters. It is evident from Fig. S14a that  $\rho_{\square}$  saturates at a slightly higher temperature for the GB region as compared to the SG region, which manifests in a relatively high Kondo temperature  $T_K \sim 20$  K). Fitting the resistivity data for the GB region at  $n = -6 \times 10^{12} \text{ cm}^{-2}$  with Eq. 4, we get  $\rho_c \approx 0.11(h/e^2)$ ,  $\rho_{K,0} \approx 0.05(h/e^2)$ ,  $A \approx 0.47$  and  $T_K \approx 20$  K respectively. Finally, Fig. S14b compares the relative contribution of the  $e$ - $e$  interaction-induced corrections  $\rho_{e-e}$  (green solid line) and the Kondo contribution  $\rho_K$  (purple solid line) to the total experimental value (red circles) obtained for the GB region at  $n = -6 \times 10^{12} \text{ cm}^{-2}$ .

## S12. Temperature dependence of noise $N = S_\sigma/\sigma^2$

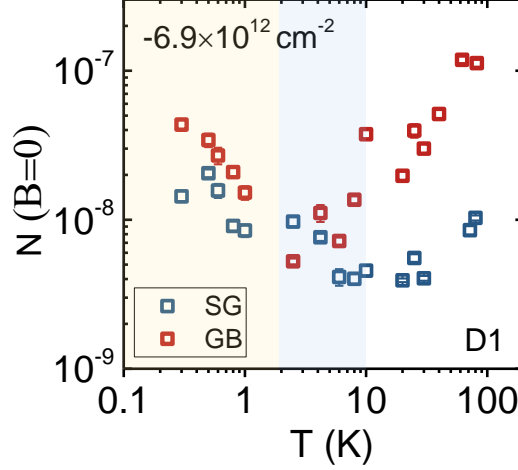


Figure S15. Normalized variance  $N = S_\sigma/\sigma^2$  at  $B = 0$  as a function of temperature is plotted for SG (blue) and GB (red) regions at  $n = -6.9 \times 10^{12} \text{ cm}^{-2}$  for device D1.

The noise  $N = S_\sigma/\sigma^2$  at  $B = 0$  in both the SG and GB regions of D1 at  $n = -6.9 \times 10^{12} \text{ cm}^{-2}$  (Fig. S15) show clear non-monotonic temperature dependences. The noise initially decreases as the temperature is lowered in an almost linear fashion ( $\propto T$ ) as expected from the noise models based on carrier tunneling between the channel and trap states spread over an energy range  $\sim k_B T$  about the Fermi energy. Below  $T \approx 10 \text{ K}$  (which matches with the temperature scale in Fig. S7a), quantum interference contributions can no longer be neglected, and the increase in SG noise with decreasing  $T$  can be explained using the Feng-Lee-Stone (FLS) theory of UCF noise [18]. However, the comparatively sharper increase in noise of the GB region below  $T \approx 2 \text{ K}$  cannot be attributed to conventional FLS theory alone. This temperature scale matches with both the observed spontaneous breaking of TRS in magneto-noise and the resistivity downturn in the time-averaged equilibrium resistance, and can be explained through the drastic increase in chaotic spin ensemble configurations in the spin glass phase [19].

- 
- [1] P. A. Lee, A. D. Stone, and H. Fukuyama, Phys. Rev. B **35**, 1039 (1987).
  - [2] J. M. Soler, E. Artacho, J. D. Gale, A. García, J. Junquera, P. Ordejón, and D. Sánchez-Portal, J. Phys.: Condens. Matter **14**, 2745 (2002).

- [3] N. Troullier and J. L. Martins, Phys. Rev. B **43**, 1993 (1991).
- [4] J. P. Perdew, K. Burke, and M. Ernzerhof, Phys. Rev. Lett. **77**, 3865 (1996).
- [5] V. Kochat, C. S. Tiwary, T. Biswas, G. Ramalingam, K. Hsieh, K. Chattopadhyay, S. Raghavan, M. Jain, and A. Ghosh, Nano Lett. **16**, 562 (2016).
- [6] A. Ghosh, S. Kar, A. Bid, and A. Raychaudhuri, arXiv preprint cond-mat/0402130 (2004).
- [7] E. McCann, K. Kechedzhi, V. I. Fal'ko, H. Suzuura, T. Ando, and B. L. Al'tshuler, Phys. Rev. Lett. **97**, 146805 (2006).
- [8] A. N. Pal, V. Kochat, and A. Ghosh, Phys. Rev. Lett. **109**, 196601 (2012).
- [9] V. Kochat, *Impact of disorder, magnetism and proximity-induced superconductivity on conductance fluctuations in graphene* (PhD Thesis, Indian Insitute of Science, India, 2014).
- [10] A. Trionfi, S. Lee, and D. Natelson, Phys. Rev. B **70**, 041304 (2004).
- [11] S. S. Alexandre, A. D. Lúcio, A. H. Castro Neto, and R. W. Nunes, Nano Lett. **12**, 5097 (2012).
- [12] L. Kou, C. Tang, W. Guo, and C. Chen, ACS Nano **5**, 1012 (2011).
- [13] A. Cortijo and M. A. Vozmediano, Nucl. Phys. B **763**, 293 (2007).
- [14] S. Lara-Avila, A. Tzalenchuk, S. Kubatkin, R. Yakimova, T. Janssen, K. Cedergren, T. Bergsten, and V. Fal'ko, Phys. Rev. Lett. **107**, 166602 (2011).
- [15] J. Jobst, D. Waldmann, I. V. Gornyi, A. D. Mirlin, and H. B. Weber, Phys. Rev. Lett. **108**, 106601 (2012).
- [16] J.-H. Chen, L. Li, W. G. Cullen, E. D. Williams, and M. S. Fuhrer, Nat. Phys. **7**, 535 (2011).
- [17] D. Goldhaber-Gordon, J. Göres, M. A. Kastner, H. Shtrikman, D. Mahalu, and U. Meirav, Phys. Rev. Lett. **81**, 5225 (1998).
- [18] S. Feng, P. A. Lee, and A. D. Stone, Phys. Rev. Lett. **56**, 1960 (1986).
- [19] S. Feng, A. J. Bray, P. A. Lee, and M. A. Moore, Phys. Rev. B **36**, 5624 (1987).